


Fracture Behavior and Fatigue Performance of Inconel 625

Fábio Gustavo Lima Pereira^a, Jorge Magner Lourenço^{b*}, Rubens Maribondo do Nascimento^a,
Nicolau Apoena Castro^a

^aPrograma de Pós-Graduação em Ciências e Engenharia de Materiais Natal, Universidade Federal do Rio Grande do Norte - UFRN, Natal, RN, Brasil.

^bInstituto Federal de Educação Ciência e Tecnologia do Rio Grande do Norte, Natal, RN, Brasil

Received: December 12, 2017; Revised: March 14, 2018; Accepted: May 06, 2018

Inconel 625 is a nickel-based highly-resistant superalloy widely used in aerospace components, in the nuclear industry, and especially in the maritime industry. Materials such as Inconel 625 have been widely used in oil exploration of Brazilian pre-salt layers due to their excellent resistance to corrosion under tension, pitting and crevice corrosion by chloride and sulphide ions, and also because they are resistant to microbiological corrosion. All components used in the exploration of crude oil in these environments suffer mechanical fatigue from oceanic oscillations that naturally occur. Samples were precisely machined and tested under uniaxial tension and cyclic tension-compression fatigue following determinations of the ASTM E8M and ASTM E466 standards respectively, at a loading ratio of $R = -1$. Tensile strengths of 586, 472, 382 and 306 MPa were selected according to the yield strength of the material for raising the S-N curve. A macro and microstructural characterization regarding failure modes was performed revealing that fatigue striations predominated in the stable region of crack growth, whereas microvoids coalescence prevailed in the fast fracture zone. Inconel 625 presented a refined microstructure composed of equiaxial grains with a mean size of 14 μm , typical of refining obtained by hardening followed by recrystallization. The precipitation of MC type carbides ($M=\text{Mo}$ or $M=\text{Nb}$) and Cr_{23}C_6 dispersed in the austenitic matrix of Inconel 625 controls a secondary alloy hardening mechanism.

Keywords: *Fatigue Behavior; Fracture Mechanism, Inconel 625.*

1. Introduction

One of the major engineering challenges today is the development of materials capable of withstanding the most diverse types of mechanical demands in harsh environments. Since the mid-1960s, several alloys with different chemical compositions have been developed with the purpose of meeting the demand of the aerospace, automobile, and above all the petrochemical industries¹. A greater prominence is given to nickel-based alloys for these applications, commonly called superalloys, and among which Inconel 625 can be highlighted. The properties that make this alloy an excellent choice to be used in harsh environments (such as for application in oceanic waters) include an environment free from pitting and crevice corrosion, high resistance to corrosion by fatigue, high resistance to corrosion under tension due to the presence of chloride and sulphide ions, and resistance to microbiological and CO_2 corrosion². In addition to good behavior under aggressive environments, this material exhibits high resistance to thermal fatigue and excellent weldability³. Inconel 625 metal powder has also been routinely used by deposition according to the laser cladding process to repair damaged components, providing superior repair when compared to the traditional GTAW process⁴. Inconel 625 is an austenitic nickel-based superalloy with cubic crystalline face-centered

structure, hardened by solid solution from the addition of chemical elements such as molybdenum and niobium in the nickel-chromium matrix which provides high resistance to the material without the need for specific heat treatments or precipitation of intermetallic compounds⁵. This alloy may also contain carbides in the form of MC, M_6C and M_{23}C_6 , rich in Nb, Mo and Cr⁶. Above all, this particular material stands out due to its excellent characteristics which include a combination of good ductility with high tensile and creep resistance, as well as high resistance to high temperatures, even when exposed to severe environments for extended periods^{7,8}. Given this combination of mechanical properties, one of the possible applications of these materials would be as structural components in the pre-salt industry.

Pre-salt is an area of oil reserves found under a deep layer of salt rock, which forms one of the several rock layers under the marine subsoil⁹. Exploring crude oil from these reserves requires materials capable of withstanding extreme conditions such as high temperature and pressure, high levels of corrosion, and mainly being subject to fatigue resulting from the action of marine currents (for example). The fatigue process currently accounts for most of the failures observed in mechanical components, and it is a critical factor since it causes premature failure of materials¹⁰. However, some

* e-mail: jorge.magner@ifrn.edu.br

aspects related to fatigue behavior and the failure mechanism of nickel-based superalloys, specifically that of Inconel 625, can be considered open issues in the present literature. The purpose of this paper is to investigate the fatigue behavior of Inconel 625 in determining its S-N curve - applied stress versus number of cycles - when subjected to a traction-compression cyclic loading at a loading ratio of $R = -1$. Moreover, a detailed investigation was carried out regarding its main failure mechanisms in order to address an existing gap in the literature, in addition to a microstructural characterization using field emission scanning electron microscopy.

Microstructure, hardness and tensile strength analyses were also evaluated to complement the microstructural and mechanical characterization of Inconel 625. Fatigue-fractured surfaces were carefully examined, relating the different loading levels to the failure modes.

2. Experimental Procedure

2.1 Base material

The material used for this study was commercial nickel-based superalloy (Inconel 625) round bars with diameter of 33 mm and chemical composition as shown in Table 1. It was supplied by Villares Metals S/A and produced by hot rolling and annealed at 910°C for two hours.

2.2 Tensile and hardness tests

The tensile test was performed on a Shimadzu AG-X series servo-electric testing machine with a capacity of 100 kN. The test was performed according to the ASTM E8M-08 standard¹¹. Three specimens with standardized shape and dimensions were prepared in a CNC machine, as shown in Fig. 1a. These samples were treated with #220 to #1500 sandpaper to ensure the removal of the marks inherent to the machining.

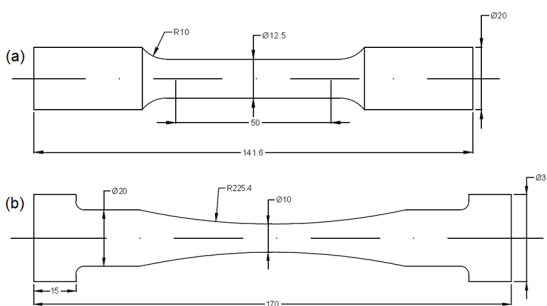


Figure 1. Dimensions of the Inconel 625 test specimens (a) tensile test (b) fatigue test.

Table 1. Chemical composition (% by weight).

	Ni	Cr	Mo	Nb	Fe	Al	Ti	Ta	Si	Co	Mn	C
Inconel 625	66.6	20.47	8.15	3.49	0.63	0.27	0.192	< 0.05	0.04	0.03	0.01	0.019

Hardness measurements were performed using a model HPO 250 Rockwell C hardness measuring equipment by WPM. A pre-load of 10 kgf was applied and maintained for 10 seconds, followed by the application of a 150 kgf load according to the standard procedure established by the ASTM E18-16 standard¹².

2.3 Fatigue testing samples

Each fatigue test specimen was prepared in accordance with the standard ASTM E466-15¹³ (according to the dimensions shown in Fig. 1b). The specimens are button-head connection type in order to obey the mechanical tightening of the coupling flange of the servo-hydraulic. The stress concentration factor k_t is approximately 1.04 for this sample type¹⁴. Fifteen specimens were prepared in a CNC machine, of which three samples were tested at each of the five loading levels (ie each stress level had 66.7% of replication) in order to achieve statistical reliability of the data. The number of samples was based on ASTM E739-10¹⁵ for design allowables data.

The specimens were treated by using #220 to #1500 granulometry sandpaper and polished with 1µm diamond paste for the removal of marks inherent to the machining, and thus to guarantee the necessary surface finishing. Surface roughness measurements for all samples were: $R_a = 0.2$ µm. These measurements were made using Taylor Hobson Surtronic 25 measuring equipment.

2.4 Constant amplitude loading history

Fatigue tests were performed in accordance with standard ASTM E466-15¹³ for fatigue tests with tension-compression uniaxial cyclic loading under constant stress amplitude for the proper analysis of the Inconel 625 S-N curve. The tests were carried out at room temperature. A universal Shimadzu EHF series servo-hydraulic testing machine equipped with a load cell of 250 kN was used to apply fatigue loading with constant amplitude at a loading ratio of $R = -1$ and a frequency of 10 Hz. Tests were performed using sinusoidal waveform power control.

The analysis strategy consisted of initially performing the tests with the specimen submitted to a load corresponding to the yield strength of Inconel 625. Load values were thereafter determined based on the yield strength of the material and its behavior when subjected to the previously analyzed loading level. Table 2 shows the loading levels used for developing the Inconel 625 S-N curve. The number of cycles to failure for each stress level was determined as the cycle in which the final fracture occurs. The limit of the number of cycles (for which infinite life was considered) was defined as being equal to 10^7 cycles¹⁶.

Table 2. Loading amplitude levels used for the fatigue tests.

Loading amplitude (MPa)	yield strength %
472	100%
586	125%
382	81%
306	65%
240	50%

Analysis of fatigue data assumes that the S-N curve can be represented as an inclined straight line in the finite life region in log-log coordinates. In the stress-based approach, the Basquin relation is the most indicated equation to represent the S-N curve:

$$S_a = A \times (2N_f)^b \quad (1)$$

where b is the fatigue strength exponent and A is the fatigue strength coefficient.

The fatigue limit will be estimated through statistical analysis based on the staircase method. For this analysis will be considered the samples submitted to the three loading levels near the infinite fatigue life region, this loading amplitudes are shown in the table 2.

2.5 Fractographic analysis

The fracture surface ends of each of the tested fatigue samples were cut using an Arocor 40 type abrasive cutting blade machine from Arotec Industria Ltda. Fractured surface cleaning was performed by ultrasound in an alcohol-based solution using UltraCleaner 1650 equipment for about six minutes.

The macroscopic appearance of the fracture surfaces were analyzed using an Olympus stereoscopic loupe. Larger magnitude images of the fracture surfaces were obtained using a scanning electron microscope equipped with an energy dispersive X-ray spectrometer (440i, LEO ElectronMicroscopy). The analyses were carried out under 20 KV stress acceleration and the images were obtained via secondary electron detector.

2.6 Microstructural characterization

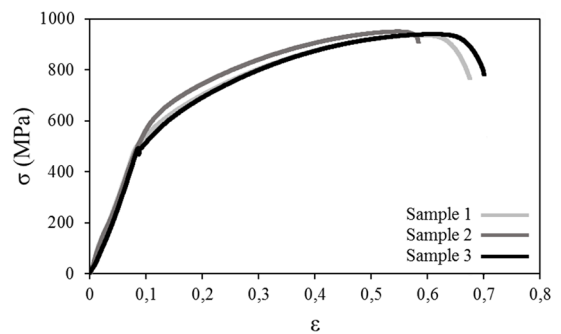
The sample used in the microstructural analysis was taken from a cross section region of the laminated bar, treated by sanding with #220 to #1200 sandpaper and polished in a diamond suspension, followed by final polishing by immersion in colloidal silica. A Zeiss Auriga 40 field-emission scanning electron microscope (FESEM) was also used, from which images were obtained by an Energy Selective Backscatter (EsB) electron detector

and via EBSD, acquiring the images via an FSD detector (Forescatter Detector) and quality map of backscattered electron diffraction pattern. Chemical analyses using energy dispersive spectroscopy (EDS) were also carried out.

3. Results and Discussion

3.1 Tensile and hardness tests

The tensile test results are summarized in Table 3. The obtained values were similar to those presented in the material certificate provided by Vilares Metals S.A. The stress-strain curves obtained for the standardized test specimens that were tested are compared in Figure 2. Table 3 also shows the mean and standard deviation of Inconel 625 Rockwell C hardness measurements.

**Figure 2.** Tension-deformation curve obtained by the standardized test.

Preliminary analysis of annealed Inconel 625 mechanical properties shows that the main characteristic of this material is an association of high mechanical resistance and moderate hardness with good ductility. In fact, the measured yield strength and tensile strength were 472 MPa and 935 MPa, respectively, and the hardness was equal to 21 HRC. The mean percentage elongation (a measurement of the material's ductility) between the three specimens tested was 56,4% (elongations of 27, 29.5 and 28,1 mm were observed). Moreover, the estimated modulus of elasticity was 205 GPa. Ramkumar et al.⁶ found similar results.

3.2 Microstructural characterization

Below are the images of Inconel 625 obtained by EBSD. It is worth pointing out that no effective method to perform a metallographic attack was found due to the material's high resistance to corrosion. As EBSD analyses provide microstructural identification through parameters related to the material's crystalline network, this technique represented a very efficient option in characterizing the alloy. Figure 3 a

Table 3. Results obtained for the tensile and Rockwell C hardness tests.

Tensile strength [MPa]	Yield strength [MPa]	Modulus of elasticity [GPa]	Elongation [%]	Hardness [HRC]
935	472	205	57	21±1

presents an image via FSD (forescatter detector) of the polished section of the sample. The color pattern is obtained via channeling effect, which promotes electron scattering at angles that depend on grain orientation. An RGB (red, green, blue) scale was applied to this effect, providing an image whose colors depend on the grain orientation, making it possible to visualize the microstructure of the material even without metallographic attack.

Figure 3 b shows a diffraction pattern quality map of backscattered electrons (in grayscale) with grain boundary mapping (regions between orientations with angular difference greater than 10° presented by the black lines)

and twin crystals ($\Sigma 3$, with 60° rotation around the $\langle 111 \rangle$ axis, represented by red lines), common in FCC crystalline structure materials such as nickel superalloys¹⁶. The images provide a visualization of the microstructure consisting of equiaxed grains, with annealing twin crystals. Mean grain size was also calculated from the EBSD maps, in which twin crystal boundaries were disregarded since low energy contours contributed little to the material hardening. The distribution curve of equivalent grain diameters is shown in Figure 4, from which the average grain diameter of $14 \mu\text{m}$ was calculated. This grain size is typical of Inconel 625, and is obtained by hardening followed by recrystallization,

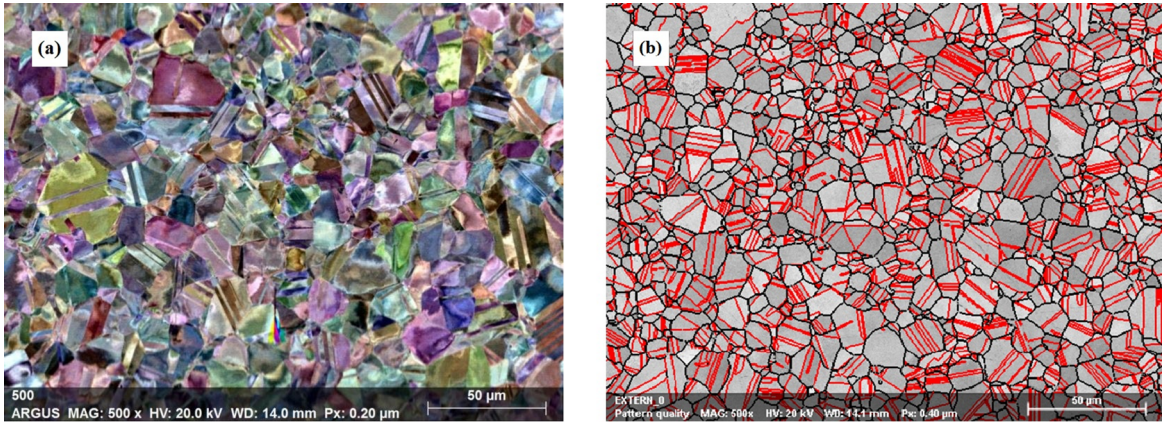


Figure 3. (a) Microstructure of Inconel 625 grains observed by EBSD/FSD. The color scale was obtained through the channeling effect, which provides an identification of the grain structure, even without metallographic attack. (b) Quality map of backscattered electron diffraction pattern with grain boundary mapping (black lines, indicating difference of orientations greater than 10°) and twin boundaries (red lines, indicating special outline $\Sigma 3$, obeying the rotation orientation relationship of 60° around the $\langle 111 \rangle$ axis).

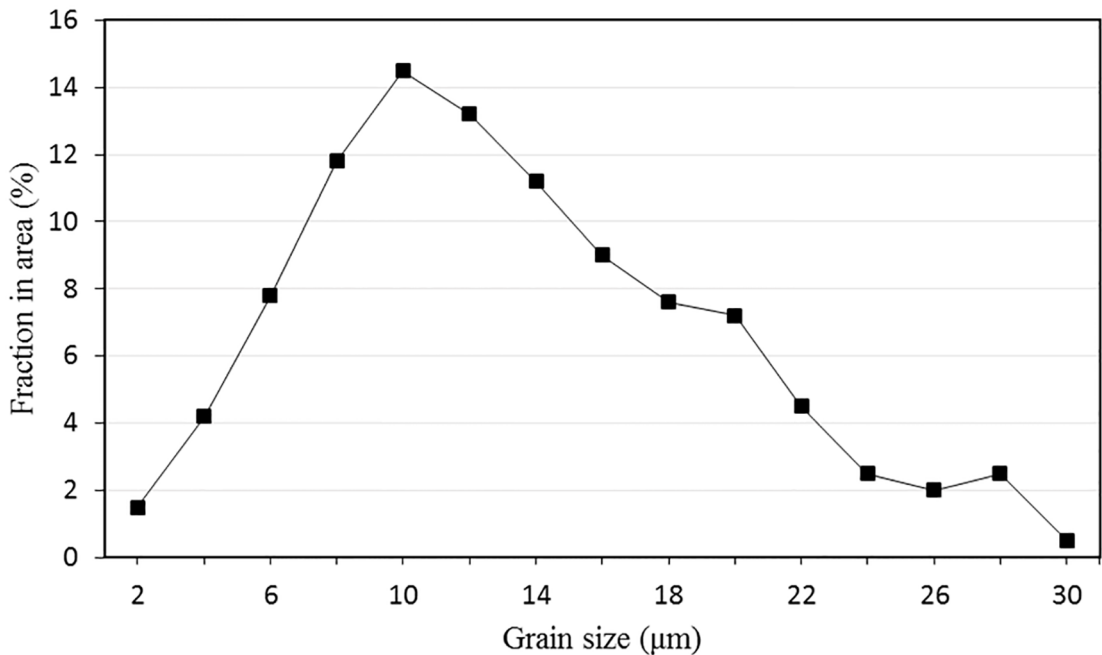


Figure 4. Equivalent diameter distribution of Inconel 625 annealed grains obtained by EBSD, with mean value of $14 \mu\text{m}$.

being the main procedure for grain refining in these alloys. In general, hot rolled Inconel 625 presents a microstructure with a mean grain size to the order of 50 μm . Grain refining is achieved by performing the heat treatment at the appropriate temperature. The Inconel 625 can obtain refined grain structures resulting from the fixing effect of carbide particles in the grain boundary, when heat treated in the temperature range between 900 and 1050 $^{\circ}\text{C}$.

As will be demonstrated later, the presence of carbides dispersed in grain contours can effectively inhibit the grain growth process based on the following mechanism: in polycrystalline alloys containing immobilizer particles (carbides) when the grain boundary intersects one of these particles it spontaneously absorbs them in order to achieve a state of lower energy. On the other hand, increasing the grain boundary area tries to increase energy, which hinders the later movement of grain boundaries³. This process can confer greater resistance to the alloy due to increased grain refining resistance, and an excellent combination of corrosion resistance and mechanical properties. The solid solution hardening effect of these elements is the main reinforcing mechanism of Inconel 625⁸.

Figures 5a and 5b show the MC and M_{23}C_6 precipitates found using the EBSD technique through punctual analyses of the diffraction pattern. In addition to solid solution hardening, a secondary hardening mechanism has been observed which contributes to its increased material strength, maintaining its hardness from the precipitation of these MC (M=Mo or M=Nb) and M_{23}C_6 (M = chrome) type carbides dispersed in the austenitic matrix. Rai et al.¹⁷ also found the formation of primary carbides in Inconel 625 in the annealed condition. It is verified that the MC carbide precipitation with block formation morphology occurred along both the grain boundaries and within the grains, while M_{23}C_6 precipitate is found dispersed along the grain contours with a finer morphology. Identification of these precipitates was carried out with the aid of the energy-dispersive X-ray spectroscopy (EDS). EDS allowed us to determine the chemical composition of different regions and precipitates found along the microstructure of the material, similar to those shown in Figures 6a and 6b. It is important to note that the carbon content was not quantified due to the limitation of the technique in quantifying elements with low atomic mass. The values presented in Table 4 are semi-quantitative.

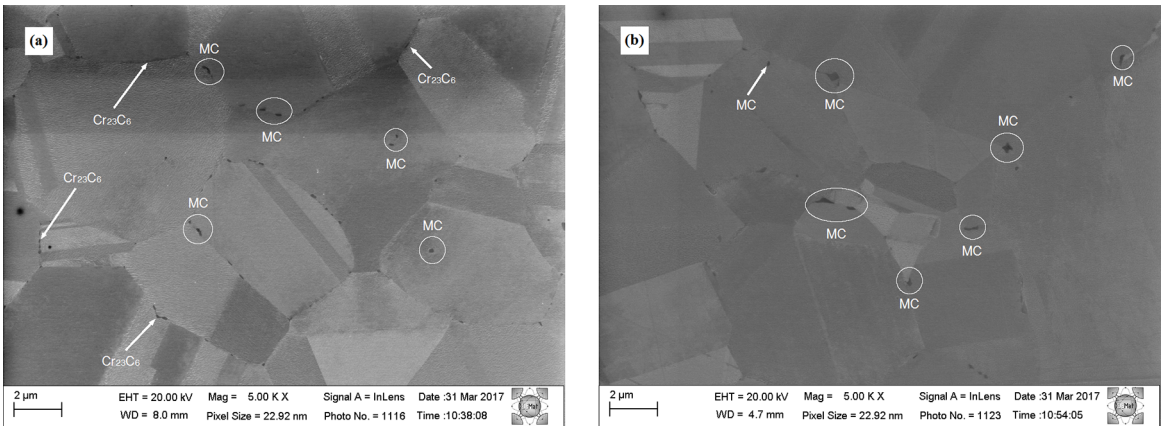


Figure 5. Images obtained by detection of secondary electrons from regions with precipitates previously identified by EBSD (a) MC and M_{23}C_6 precipitates and (b) MC precipitate found.

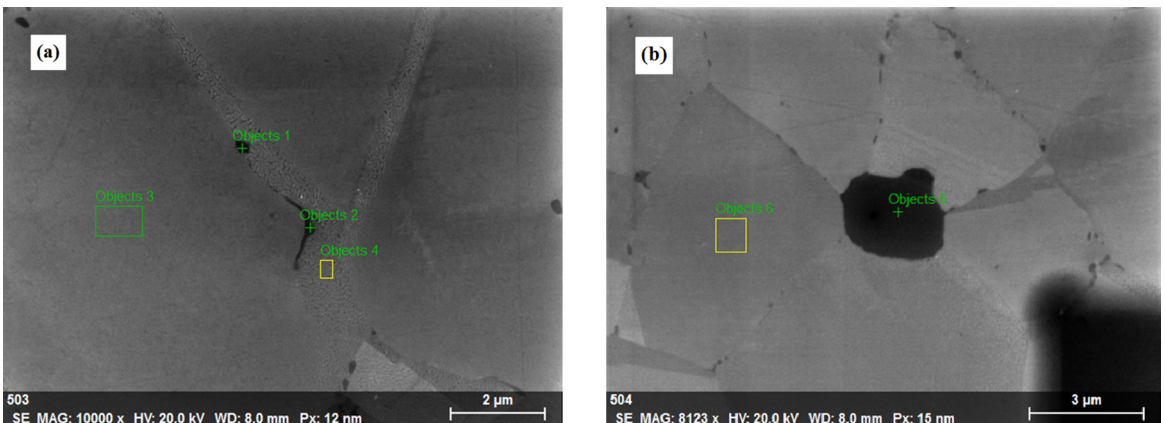


Figure 6. Images obtained by detection of secondary electrons from regions analyzed by EDS (a) objects 1, 2, 3 and 4 and (b) objects 5 and 6.

Table 4. Chemical composition (% by weight) of the analysed regions and precipitates

Object	Al	Ti	Cr	Ni	Nb	S
1	0.25	1.34	18.46	54.29	25.66	-
2	0.21	1.40	17.63	50.75	30.01	-
3	0.3	-	23.19	66.54	5.34	4.62
4	0.29	-	22.96	66.13	5.96	4.65
5	-	1.98	0.93	2.82	94.27	-
6	0.32	-	22.84	66.33	5.89	4.62

In analyzing the morphology of the microstructure, two predominantly distinct regions can be observed, namely the austenitic matrix (lighter regions) and the precipitates (darker regions). The analysed and highlighted objects in Figures 6a and 6b show the composition shown in Table 4. Regions corresponding to the austenitic matrix (objects 3, 4 and 6) have a predominance of nickel and chromium (around 66% and 23%, respectively) and about 5% niobium content, which was expected since the γ phase is formed from the solid solution obtained by the addition of alloy elements such as chromium. In relation to the precipitates (objects 1, 2 and 5), the EDS analysis indicated that such compounds are rich in Ni, Cr, and especially niobium (reaching 94.27% in object 5). Ni, Cr and Mo elements are major constituents of the alloy and may appear at relatively high levels due to the interaction of the electron beam with the matrix, even when the analysis point is on/over the precipitate. The presence of titanium was also observed, which is an element known to be a strong carbide builder. Since it is a light chemical element which generates difficulties and errors in the quantification process, the presence of carbon in the composition was not identified; however, the niobium content suggests that precipitates are actually Nb-rich carbides.

Precipitation of second-phase compounds such as $M_{23}C_6$ occurs selectively throughout the grain boundaries¹⁸. The morphology and precipitation kinetics of these carbides are closely related to the lack of orientation of the grain boundaries¹⁹. In addition, they tend to precipitate first in high-angle grain contours at random and then on inconsistent interfaces²⁰. However, to date it is still not clear why the morphology of $M_{23}C_6$ carbide is different among different types of grain boundaries in the most diverse alloys. This behavior needs to be investigated in future studies.

As mentioned earlier, the main observed feature of Inconel 625 is its ability to exhibit high mechanical strength without impairing its ductility. This characteristic is related to the influence of the $M_{23}C_6$ carbide on these mechanical properties. Lee et al.¹⁸ concluded that the tensile strength and ductility of Inconel were reduced when the material underwent an aging heat treatment. This fact is mainly related to the breaking of $M_{23}C_6$ carbides. The morphology of these compounds is the main influencing factor on the mechanical properties of these materials. The distribution of these carbides, being harder and more fragile compounds than the γ matrix with sizes smaller than 0.5 μm in a discontinuous chain along the grain contours, prevents the

growth of brittle fracture cracks while not interfering in the ductility due to the deformations that they cause in the grain contour regions^{21,22}. Thus, they act by preventing voids from coalescing, which prevents excessive dislocation movement.

3.3 Fatigue behavior

The statistical analysis assumes that the resulted fatigue life $2N_f$ follows the lognormal distribution for a stress amplitude S_a ²³. From eq. (1) by taking logarithms for both sides and using the least-squares method, the fatigue strength coefficient (A) and fatigue strength exponent (b) were obtained for S-N curve (stress amplitude/reversals to failure) plotted in Fig. 7, which also shows the lower bound S-N curve for Inconel 625. Those constants are shown in table 5 and in the following relation:

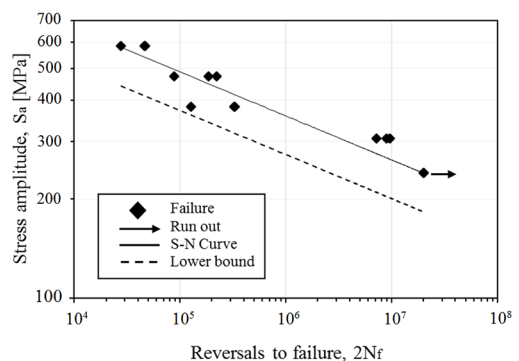
$$S_a = 2282(2N_f)^{-0.134} \quad (2)$$

In addition, two statistical fatigue properties were derived from least-squares method:

$$s = 0.3248 \text{ and } C_s = \sqrt{10^{b^2 s^2} - 1} = 0.0661 \quad (3)$$

where s is the standard sample deviation of $\log(2N_f)$ and C_s is the coefficient of variation of the fatigue strength coefficient.

The lower bound of the S-N curve was determined using the Owen one-side tolerance limit approach presented by Shen, Wirshing and Cashman²⁴. Indeed, the lower bound in log-log coordinates can be constructed by a line with the same fatigue strength exponent b from the original S-N curve that is

**Figure 7.** Fatigue test results.

horizontally shifting to the left from the median baseline with a quantity $s \times K_{Owen}$. Where K_{Owen} factor are tabled in Williams, Lee and Rilly²⁵ and s was determined in the eq. (3). For sample size $n_s = 15$, 95% probability of survival and 95% confidence level yields to $K_{Owen} = 2.712$. The results of constants for the lower bound curve are also shown in Table 5.

Table 5. Basquin's constants equation and upper and lower bound constants S-N curve for 95% confidence level

Constant	Estimated value	Lower bound
A	2282	1740
b	-0.134	-0.134

For all analysed loading levels, the specimens withstood the same magnitude order of cycle's number when submitted to certain levels of stress amplitude. The specimens tested at a stress amplitude of 240 MPa did not present fracture, even when subjected to 10^7 cycles, which is the limit set as reference for infinite life. As mentioned in section 2.4, the behavior when subjected to the previously analyzed stress level was taken into account to choose the next loading level. Therefore the experiments were conducted by decreasing or increasing the stress level with a mean step $d = 66$, depending on the previous test result (failure or run out).

That is the procedure established by staircase method. The staircase method is the most used fatigue test technique to estimate the fatigue limit of a material²³ and its use generates the sequence plotted in fig. 8. Considering the failure event in the statistical analysis, the data reduction technique proposed by Dixon and Mood²⁶ is used for fatigue limit estimation. The failure events at the stress levels σ_i are denoted by n_i ($n_0 = 0, n_1 = 3, n_2 = 1$). Where n_0, n_1, n_2 correspond to the number of failure events when samples were subjected to stress amplitudes of 240, 306 and 382 MPa, respectively. Thus, the fatigue limit in terms of stress amplitude results as the mean value calculated using the equation:

$$S_R = S_0 + d \left(\frac{\sum i n_i}{\sum n_i} + 0.5 \right) = 355.5 \quad (4)$$

with the standard deviation:

$$S_s = 0.53d = 35 \quad (5)$$

Assuming a normal distribution on the lower bound in the infinite range is determined using the expression:

$$S_{RL} = S_R - K S_s = 244 \text{ MPa} \quad (6)$$

where $K = 3.187$ for 90% probability of survival, 90% confidence level and number of failure events $n = 4$ ²⁶.

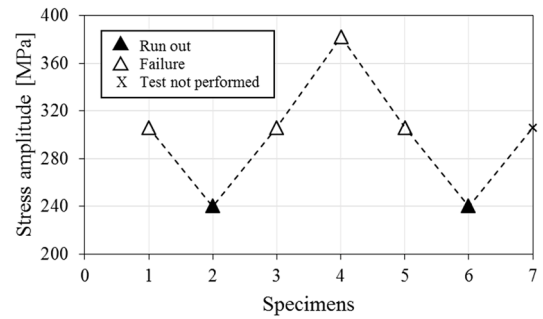


Figure 8. The staircase fatigue data.

Therefore the fatigue strength of Inconel 625 was estimated to be approximately 244 MPa under a loading ratio of $R = -1$ and considering 10^7 cycles as the limit for infinite life.

Fig. 9 shows the stable crack growth, fast fracture and shear lip regions. The beachmarks are clearly identified on the fracture surface of Inconel 625, more precisely in the stable crack growth zone. This is a typical feature of the fatigue process in materials with good ductility, such as Inconel 625.

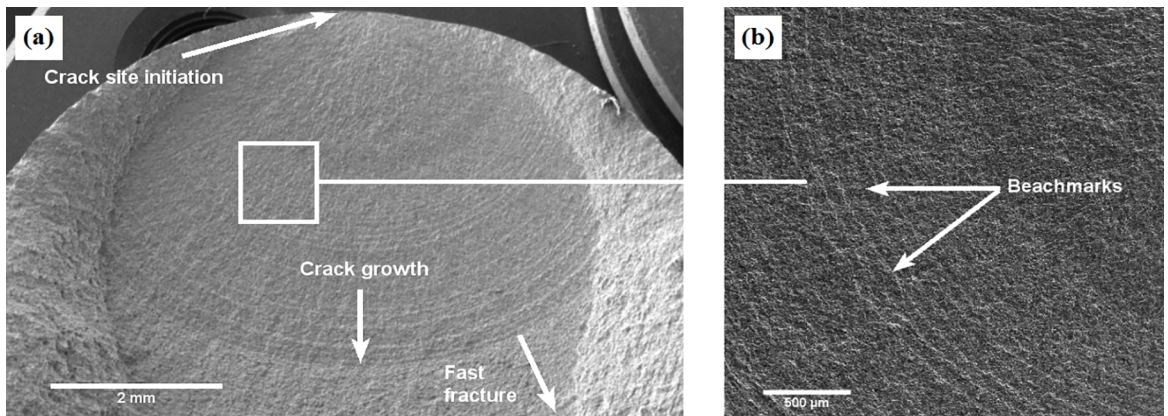


Figure 9 . Annealed Inconel 625 fracture surface showing stable crack growth region by fatigue (on the left); and an enlargement of the white square region (to the right).

3.4 Fractography

When a material is subjected to cyclic loading, many microscopic changes occur in its crystalline structure under the action of relatively low and repeated loads. These minimal changes in the structure can gradually evolve and cracks are nucleated. In the nucleation process of these cracks, thousands of fatigue cycles are consumed, thus corresponding to Stage I of the fatigue fracture process (known as initiation). Indeed, this is the most complex stage of fatigue fracture. Microcracks grow and become measurable reaching stages II and III, and then lead to the fracture of a component or structure. The final rupture may present characteristics of different failure modes, such as brittle and/or ductile fractures, depending on several factors such as the analysed material, stress levels and the environment involved²⁷. For all of these variables, fracture surfaces basically consist of three characteristic regions: stable crack growth, shear lip and fast fracture.

A detailed examination of the fractured surfaces by these cyclic loads was performed using the scanning electron microscopy technique. Observations with small increases were

used to identify specific fatigue and fast fracture regions, and gradually larger increases were used to observe these regions in order to evaluate: (a) location of the crack initiation; (b) nature, extent and severity of the microscopic growth at the beginning of the crack through the microstructure; and (c) other features present on the fractured surface.

The fatigue fracture surface micrograph for Inconel 625 tested at a maximum stress of 586 MPa resulted in a fatigue life of 23432 cycles. The failure revealed fracture morphology at 45°, which in fact corresponds to the plane of maximum shear stress as shown in Figure 10a. Macroscopically delimiting the stable crack growth and fast fracture regions is difficult due to the excess of permanent fatigue deformation in a relatively low number of cycles. In this specific case, the applied stress was 25% higher than the material's yield strength, meaning near its resistance limit. No characteristic aspects of fatigue fracture present in ductile materials such as Inconel 625 were observed (i.e. beachmarks or shear lips)²⁷.

This excess of plastic deformation leaves the material susceptible to fracture resulting in the nucleation of multiple cracks (as shown in Figure 10b), which was the main source

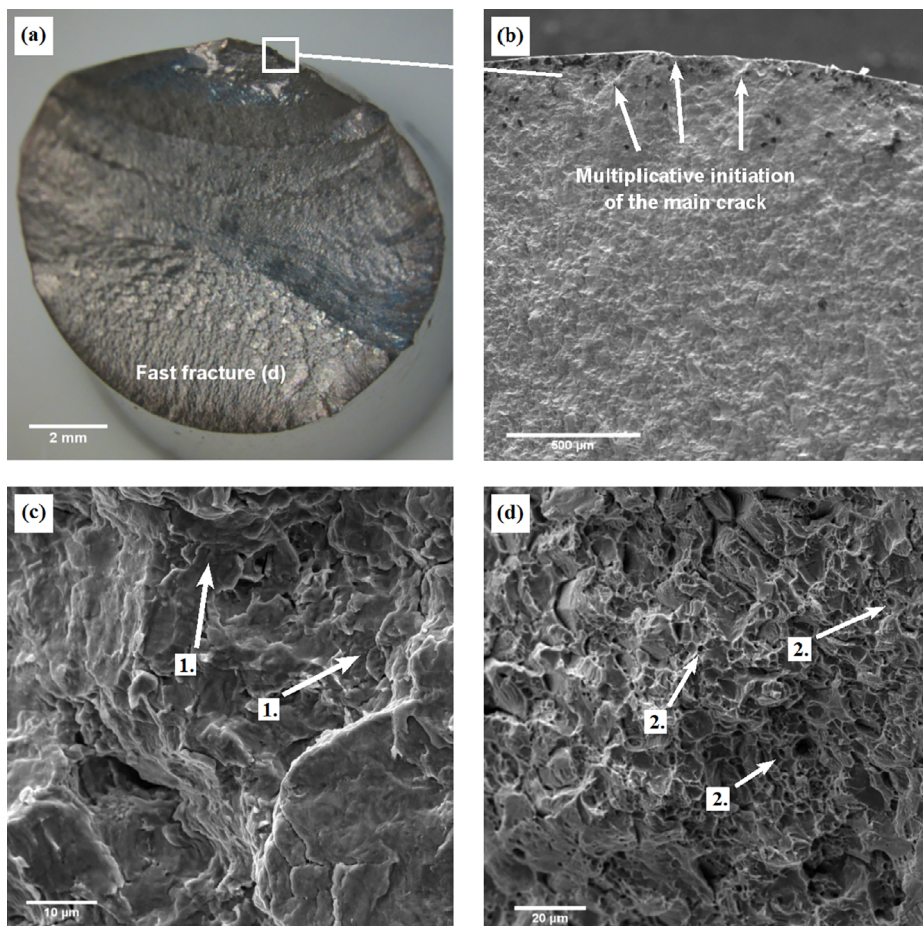


Figure 10 . Inconel 625 fracture surface after failure in 23432 cycles under maximum stress of 586 MPa: (a) appearance of the surface fracture, (b) nucleation region of the microscopic crack, (c) failure mode in the stable crack growth region, (d) failure mode in the fast fracture region.

of crack initiation. The predominant failure mode in the stable crack growth region was transgranular. Magnifying this region (shown in Figure 10c) the analysis reveals that the failure mode was shear topology²⁸. This type of fracture appears to be the result of a ductile rupture occurring on a very small scale and which leads to microcavity coalescence by plastic deformation. In many cases this results in a fracture surface that appears to have no features, which is evident in Figure 10c (number 1 indicated by arrows).

The presence of dimples is observed in the fast fracture region (number 2 in Figure 10d), which is characteristic of the fracture mode by microvoid coalescence (MVC); a ductile aspect which indicates that the final fracture stage occurred by plastic collapse. These microvoids rapidly coalesce, continuing until the fracture occurs from regions with discontinuities and localized deformations which are associated with the distribution of MC and $M_{23}C_6$ carbides. This coalescence occurs because the Inconel 625 austenitic matrix is ductile and the carbides are hard; therefore, the matrix plastically deforms around the carbides resulting in microcavities²⁷.

Figure 11 shows the fracture surface of the sample subjected to a maximum stress of 472 MPa. The macroscopic aspect of

the failure has a flat morphology occurring at 90° from the main loading axis. There is no clear delineation between the stable crack growth and fast fracture regions. The fast fracture region can be confused with the thick shear lips; this is perceived by the fact that the stable fatigue region never extends onto these shear lips. This loading level represents the yield strength of Inconel 625, thus the fracture presents some typical macroscopic aspects of a fatigue failure (see Figure 11 a), such as some beachmarks. A crack is nucleated in microscopic discontinuity on top of the specimen's surface (region detailed in Figure 11 b). Examining the stable crack growth zone with higher magnification reveals the presence of fatigue striations (see Figure 11 c) leading in the same direction from the crack nucleation point. Fatigue striations are microscopic evidence of fatigue failure. Each time the crack is opened by stress in a fatigue cycle, the tip of the crack plastically deforms, leading to microscopic hardening (blunting) in this region. This effect causes the fracture, leaving striations on the faces of the ruptured sample. Fatigue striations are not found in high strength materials mainly due their low ductility. However, low hardness metals also do not form easily-observed striations, since the low resistance leaves the materials vulnerable to fatigue damage.

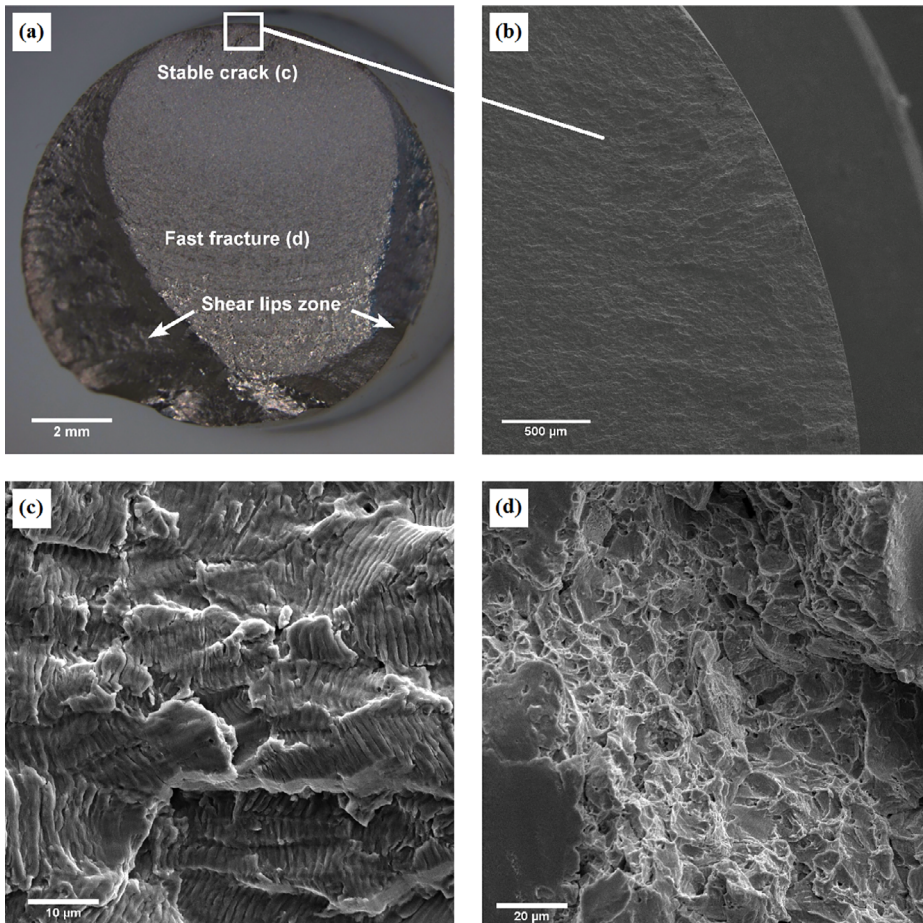


Figure 11 . Inconel 625 fracture surface after failure at 110067 cycles under maximum stress of 472 MPa: (a) appearance of the fracture surface, (b) microscopic crack nucleation region, (c) failure mode in the stable crack growth region, (d) failure mode in the fast fracture region.

Comparatively, hardened steels with hardness above 50 HRC do not develop striations²⁷. Inconel 625 presented evident and spaced fatigue striations, perhaps since it has not been characterized as either a hard or a soft material, meaning that it should have an intermediate hardness around 21 HRC, as detailed earlier. The presence of these fatigue striations proves that Inconel 625 has a unique combination of mechanical properties; even when it undergoes hardening processes and has a high resistance limit, it has the required ductility to form fatigue striations. Microvoid coalescence was also observed in the fast fracture region (as seen in Figure 11 d), similar to that observed in the sample submitted to loading of 582 MPa.

Figure 12 shows the fracture surface of a sample exposed to a maximum stress of 382 MPa; 164814 cycles were required until fracture, which allowed the formation of characteristic fatigue marks of shear lips and beachmarks, as shown in Figure 12 a. The crack was again nucleated by surface discontinuity (see Figure 12 b). The presence of high density fatigue striations (number 3 in Figure 12 c) were verified in the stable crack growth region leading in the same direction, similar to that seen in the failure mode of the sample subjected to a stress amplitude of 472 MPa. Microvoids coalescence is the predominant failure mode in the fast fracture region due to the presence of dimples (number 4 in Figure 12 e).

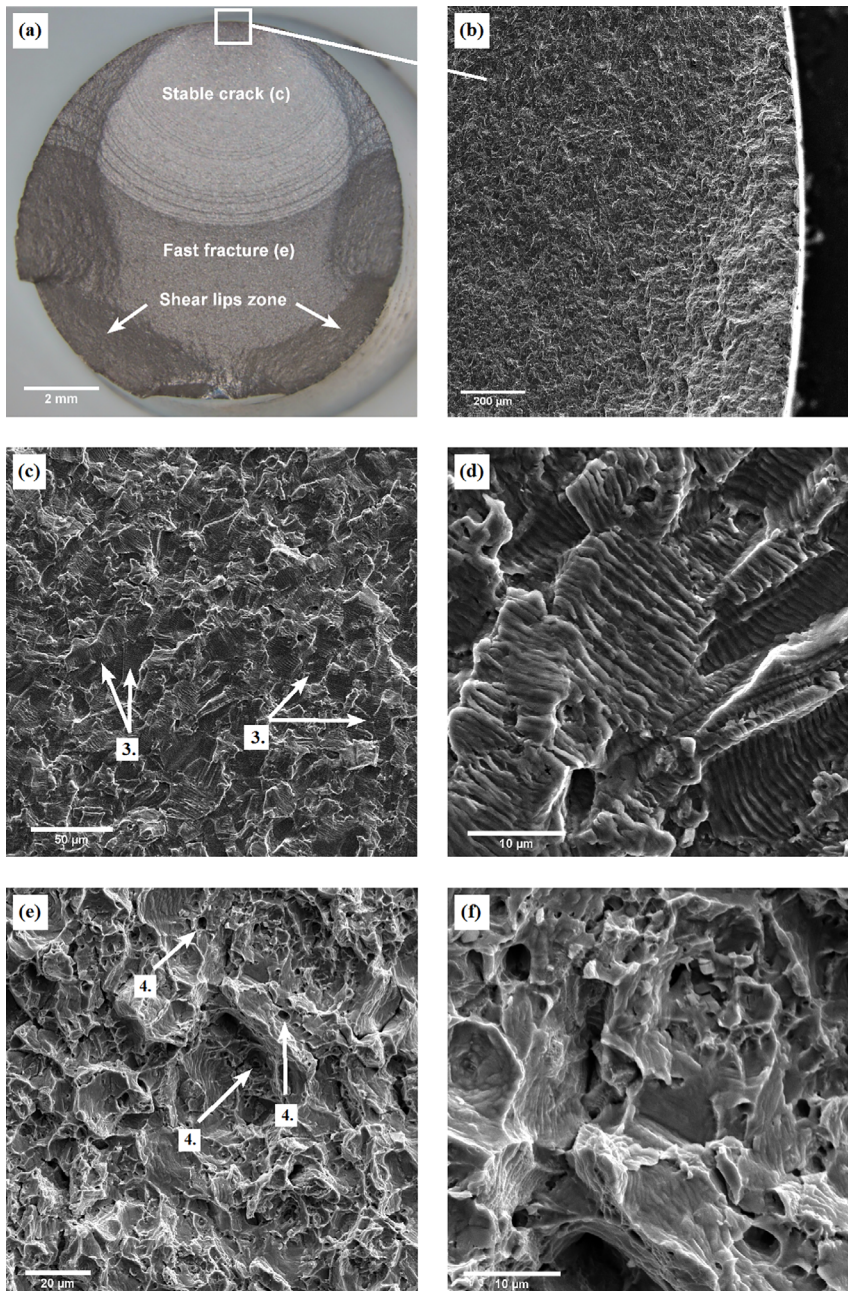


Figure 12. Inconel 625 fracture surface after failure at 164814 cycles under maximum stress of 382 MPa: (a) appearance of the fracture surface, (b) microscopic crack nucleation region, (c) failure mode in the stable crack growth region, (d) fatigue striations, (e) failure mode in the fast fracture region, (f) dimples.

For the sample submitted to stress amplitude of 306 MPa, 3599687 cycles were required until fracture. The crack nucleation region is demarcated by the white square in Figure 13 a and enlarged in Figure 13 b, showing that the crack was nucleated on the surface; a similar behavior found for the previously analysed samples. A mixture of failure modes can be observed in the stable crack growth region: cleavage, weak and spaced out fatigue striations (number 5 in Figure 13 c). The failure mode by cleavage produces some distinct characteristics on the fracture surface, such as: cleavage marks (number 6 in Figure 13 c) and river marks (item 7 in Figure 13 c) caused by the sudden separation between the faces of adjacent unit cells as the result of an overload^{16,28}. Ductile rupture is again the predominant failure mode in the fast fracture region, evidenced by the presence of dimples (see Figure 13 d).

All levels of stress amplitude applied in this analysis showed some similar fracture behaviors. In general, the cracks were nucleated from discontinuities present on the material's surface. These discontinuities act as stress concentrators and facilitate the nucleation of fatigue cracks. Moreover, the presence of macroscopic characteristics typical of fatigue were verified, such as shear lips and beachmarks for all levels of applied loading that were lower than the yield strength of Inconel 625. For these cases, fatigue was the predominant fracture mode in the stable crack propagation zone, as evidenced by the presence of fatigue striations. In fast fracture regions, the general verified behavior was fracture by microvoids coalescence, confirmed by the presence of dimples.

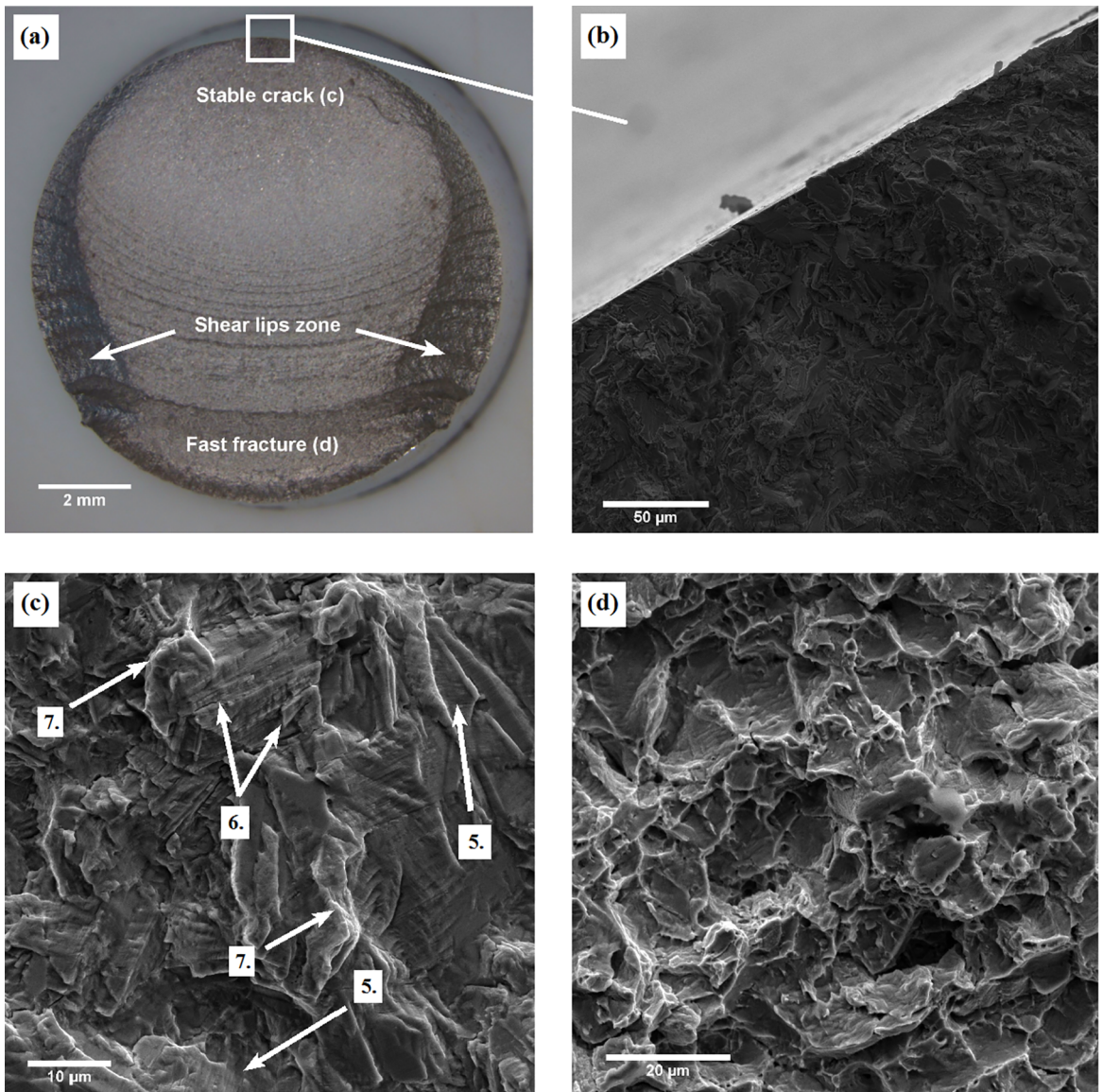


Figure 13. Inconel 625 fracture surface after failure at 3599687 cycles under maximum tension of 306 MPa: (a) appearance of the fracture surface, (b) microscopic crack nucleation region, (c) failure mode in the stable crack growth region, (d) failure mode in the fast fracture region.

4. Concluding Remarks

In this study, annealed Inconel 625 was characterized in order to understand its behavior under fatigue and fracture. Constant stress amplitude and a loading ratio of $R = -1$ were used. The microstructure and mechanical properties of Inconel were also evaluated. The following conclusions can be drawn from this study:

1. The estimated fatigue strength of Inconel 625 at a loading rate of $R = -1$ considering 10^7 cycles as the limit for infinite life was 244 MPa.
2. Fracture surface analysis showed that the cracks were nucleated from stress concentrators present on the material's surface. The failure modes in the stable crack growth regions mainly consisted of fatigue striations with Tearing Topology Surface (TTS) and cleavage areas. Finally, ductile rupture represents the main fracture mode in the final fracture or fast fracture region, where the crack becomes unstable.
3. Regarding the influence of stress amplitude on the stable crack length, it was observed that the stable growth region length increases with a decrease in stress amplitude.
4. The microstructural characterization of Inconel allowed for observing the presence of matrix phase γ and precipitation signs of MC and $M_{23}C_6$ carbides. The presence of these precipitates gave the material the ability to associate high mechanical strength and moderate hardness to good ductility, which allowed for observation of fatigue striations.

5. Acknowledgements

The authors would like to thank the financial support from the National Council for Scientific and Technological Development (CNPq) - process number: 442727/2014-3 and 158342/2015-1. The authors would also like to thank the support of the postgraduate program in materials science and engineering at UFRN and the Federal Institute of Education Science and Technology of Rio Grande do Norte (IFRN). The authors wish to record their sincere thanks to Bruna Marcela e Luciana de Castro from SEM Laboratory for their important contributions.

6. References

1. Mithilesh P, Varun D, Reddy ARG, Ramkumar KD, Arivazhagan N, Narayanan S. Investigations on Dissimilar Weldments of Inconel 625 and AISI 304. *Procedia Engineering*. 2014;75:66-70.
2. Zhang B, Bi G, Wang P, Bai J, Chew Y, Nai MS. Microstructure and mechanical properties of Inconel 625/nano-TiB₂ composite fabricated by LAAM. *Materials & Design*. 2016;111:70-79.
3. Liu M, Zheng W, Xiang J, Song Z, Pu E, Feng H. Grain Growth Behavior of Inconel 625 Superalloy. *Journal of Iron and Steel Research, International*. 2016;23(10):1111-1118.
4. Sandhu SS, Shahi AS. Metallurgical, wear and fatigue performance of Inconel 625 weld claddings. *Journal of Materials Processing Technology*. 2016;233:1-8.
5. Sims CT, Stoloff NS, Hagel WC, eds. *Superalloys II*. New York: Wiley Interscience; 1987.
6. Ramkumar KD, Abraham WS, Vijay V, Arivazhagan N, Rabel AM. Investigations on the microstructure, tensile strength and high temperature corrosion behaviour of Inconel 625 and Inconel 718 dissimilar joints. *Journal of Manufacturing Processes*. 2017;25:306-322.
7. Kim YK, Kim D, Kim HK, Oh CS, Lee BJ. An intermediate temperature creep model for Ni-based superalloys. *International Journal of Plasticity*. 2016;79:153-175.
8. Abioye TE, McCartney DG, Clare AT. Laser cladding of Inconel 625 wire for corrosion protection. *Journal of Materials Processing Technology*. 2015;217:232-240.
9. Seabra AA, Freitas GP, Polette M, Casillas TADV. A promissora provincia petrolifera do pré-sal. *Revista Direito GV*. 2011;7(1):57-74.
10. Stephens RI, Fatemi A, Stephens RR, Fuchs HO. *Metal Fatigue in Engineering*. 2nd ed. Hoboken: Wiley; 2000. p. 59-83.
11. ASTM International. *ASTM E8M-08 - Standard Test Methods for Tension Testing of Metallic Materials*. West Conshohocken: ASTM International; 2008.
12. ASTM International. *ASTM E18-16 - Standard Test Methods for Rockwell Hardness of Metallic Materials*. West Conshohocken: ASTM International; 2016.
13. ASTM International. *ASTM E466-15 - Standard Practice for Conducting Force Controlled Constant Amplitude Axial Fatigue Tests of Metallic Materials*. West Conshohocken: ASTM International; 2015.
14. Pilkey WD. *Peterson's Stress Concentration Factors*. 2nd ed. Hoboken: John Wiley & sons; 1997. p. 441-499.
15. ASTM International. *ASTM E739-10 - Standard Practice for Statistical Analysis of Linear or Linearized Stress-Life (S-N) and Strain-Life (e-N) Fatigue Data*. West Conshohocken: ASTM International; 2015.
16. Dieter GE. *Mechanical Metallurgy*. 3rd ed. London: McGraw-Hill; 1988.
17. Rai SK, Kumar A, Shankar V, Jayakumar T, Rao KBS, Raj B. Characterization of microstructures in Inconel 625 using X-ray diffraction peak broadening and lattice parameter measurements. *Scripta Materialia*. 2004;51(1):59-63.
18. Lee TH, Lee YJ, Joo SH, Nersisyan HH, Park KT, Lee JH. Intergranular M₂₃C₆ carbide precipitation behavior and its effect on mechanical properties of Inconel 690 tubes. *Metallurgical and Materials Transactions A*. 2015;46(9):4020-4026.
19. Li H, Xia S, Zhou BX, Liu WQ. C-Cr segregation at grain boundary before the carbide nucleation in Alloy 690. *Materials Characterization*. 2012;66:68-74.

20. Trillo EA, Murr LE. A TEM investigation of $M_{23}C_6$ carbide precipitation behavior on varying grain boundary misorientations in 304 stainless steels. *Journal of Materials Science*. 1998;33(5):1263-1271.
21. Andersson J. *Weldability of Precipitation Hardening Superalloys - Influence of Microstructure*. [Thesis]. Göteborg: Chalmers University of Technology; 2011.
22. Dong X, Zhang X, Du K, Zhou Y, Jin T, Ye H. Microstructure of Carbides at Grain Boundaries in Nickel Based Superalloys. *Journal of Materials Science & Technology*. 2012;28(11):1031-1038.
23. Lee YL, Pan J, Hathaway RB, Barkey ME. *Fatigue Testing and Analysis - Theory and Practice*. Burlington: Elsevier Butterworth-Heinemann; 2005.
24. Shen CL, Wirshing PH, Cashman GT. Design Curve to Characterize Fatigue Strength, *Journal of Engineering Materials and Technology*. 1996;118(4):535-541.
25. Williams CR, Lee YL, Rilly JT. A practical method for statistical analysis of strain-life fatigue data. *International Journal of Fatigue*. 2003;25(5):427-436.
26. Dixon WJ, Mood AM. A Method for Obtaining and Analyzing Sensitivity Data. *Journal of the American Statistical Association*. 1948;43(241):109-126.
27. Wulpi DJ. *Understanding How Components Fail*. 3rd ed. Materials Park: ASM International; 1999. p. 117-160.
28. Thompson AW, Chesnutt JC. Identification of a fracture mode: the tearing topography surface. *Metallurgical Transactions A*. 1979;10(8):1193-1196.